Publication IV

Ranran Lin and Antero Arkkio. 2008. 3-D finite element analysis of magnetic forces on stator end-windings of an induction machine. IEEE Transactions on Magnetics, volume 44, number 11, pages 4045-4048.

3-D Finite Element Analysis of Magnetic Forces on Stator End-Windings of an Induction Machine

Ranran Lin and Antero Arkkio

Department of Electrical Engineering, Faculty of Electronics, Communications and Automation, Helsinki University of Technology, Espoo, Finland

This paper aims to analyze the magnetic forces on the stator end-windings of an induction machine at full load by a 3-D time-harmonic finite element analysis. Under the steady-state condition, the radial, circumferential, and axial forces all consist of a constant component and a sinusoidal component with a double-frequency. The analysis shows that the forces on the knuckle part of the upper part of a coil end are larger than on the other parts and that the constant components and the amplitudes of the sinusoidal components of the forces on the same positions of different coil ends in a phase belt are nearly different. Finally, the analysis of stresses indicates that the stresses in a coil end, corresponding to the constant components of the forces, are small.

Index Terms—**End-winding, finite element analysis, force.**

I. Introduction

END-WINDINGS of a rotating electric machine, not embedded in the iron core, are subject to forces when the machine is running. Under the steady-state condition, these forces are long-term and periodic. They may cause some harmful effects on the windings, e.g. the metal fatigue, so that the insulation integrity of end-windings may be adversely affected, particularly in terms of the degradation of encapsulants.

In the past several decades, the computation of the forces on end-windings was carried out on the basis of solving the magnetic field by analytical and numerical approaches. The analytical approach mostly used Biot-Savart's law so the end-windings were replaced by infinitely thin conductors and the iron core was either neglected or modelled by using the method of images [3]–[5]. Recently, the numerical approach has been widely applied to studies that the complex end region was considered [1], [2], [6]–[9].

References [1], [2] reported the computation of the end-winding forces of large turbine generators under the steady-state and transient state conditions, respectively. The magnetic field was calculated by the finite difference method. During the steady-state computation, the variation in the forces under different power factors was explained. Besides, the fact that the circumferential forces tended to squeeze the phase belt inwards during a short-circuit fault was stated as well.

A study, reported in [3], was carried out to find the influence of the rotor current on the forces on the end-windings of an induction machine. The method of images, proposed in [4], was used in the computation of the magnetic field to remove the stator and rotor iron cores. By comparison, it was found that the rotor current could influence the distribution of the forces on the end-windings.

Some phenomena of vibrations, based upon the forces on end-windings, were also explored. Reference [5] did the analytical calculation of the forces and studied the mechanical behavior of the end-windings, e.g. the fatigue life, by calculating the strains in the end-windings. Another numerical study [6] computed the natural frequencies of the end-windings and analyzed the frequency response of the displacements. Reference [7] calculated the instantaneous forces when the phase current reached the peak value and then discussed the reliability of the support structures of the end-windings, especially the influence of the support ring.

The 3-D numerical analysis can give accurate results but it needs a large amount of computation. Therefore, a quasi-3-D finite element analysis (FEA) was applied to the computation of the forces [8], [9]. The quasi-3-D method assumes that a machine is axis-symmetric and that the field variables are sinusoidally distributed along the circumferential direction.

In this study, a commercial software package, COMSOL Multiphysics, was used to carry out the FEA of the magnetic forces as well as the corresponding stresses.

II. Numerical Simulation

A. 3-D Geometric Model

A 3-phase, 6-pole squirrel-cage induction machine working as a motor was studied here. Thanks to the symmetry and periodicity, the simulated model was only 1/12 of the machine.

The stator windings are two-layer diamond windings. A description of diamond windings can be found in [10], [11]. For the simplicity, the bent parts of the coil ends were replaced by the straight parts. In addition, each coil end was divided into 29 segments to analyze the forces. Fig. 1 shows one of the coil ends. According to the local definition here, in Fig. 1, segments 1–12 and 18–29 are termed as the lower part and upper part of a coil end, respectively. Table I lists the related specifications of the machine.

This model used a linear magnetization characteristic. The laminated iron core was anisotropic in its conductivity and permeability. The tensor of its conductivity was $2\times10^6\boldsymbol{e}_x\boldsymbol{e}_x+2\times10^6\boldsymbol{e}_y\boldsymbol{e}_y+0\boldsymbol{e}_z\boldsymbol{e}_z$ S/m and the tensor of its relative permeability was $1000\boldsymbol{e}_x\boldsymbol{e}_x+1000\boldsymbol{e}_y\boldsymbol{e}_y+50\boldsymbol{e}_z\boldsymbol{e}_z$, where $\boldsymbol{e}_x\boldsymbol{e}_x$, $\boldsymbol{e}_y\boldsymbol{e}_y$, and $\boldsymbol{e}_z\boldsymbol{e}_z$ are the unit dyads in the $x-y-z$ Cartesian coordinate system. The other structures were isotropic.

Digital Object Identifier 10.1109/TMAG.2008.2002379

Color versions of one or more of the figures in this paper are available online at http://ieeexplore.ieee.org.

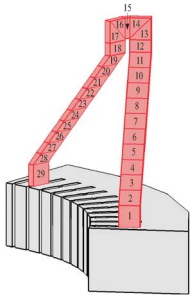

Fig. 1. The 3-D geometric model of a coil end with the indexes of the segments marked.

TABLE I
MAIN SPECIFICATIONS OF SIMULATED MACHINE

Rated power (kW)	1250
Rated frequency (Hz)	50
Rated slip	0.365%
Outer diameter of stator iron core (mm)	980
Inner diameter of stator iron core (mm)	670
Radial thickness of frame (mm)	20
Radial thickness of air-gap (mm)	3.5
Number of stator slots	72
Number of rotor slots	84
Coil span of a stator coil (stator slot pitches)	10

B. Electromagnetic Simulation by Time-Harmonic FEA

The stator windings were supplied by a current source. The general governing equation for a current source supply is

$$\nabla \times [\boldsymbol{\nu} \cdot (\nabla \times \underline{\boldsymbol{A}})] + \mathrm{j}\omega_\mathrm{s}\boldsymbol{\sigma} \cdot \underline{\boldsymbol{A}} - \underline{\boldsymbol{J}}_\mathrm{s} = 0 \tag{1}$$

where $\underline{\boldsymbol{A}}$ and $\underline{\boldsymbol{J}}_\mathrm{s}$ are complex vectors of magnetic vector potential and source current density, respectively; $\boldsymbol{\nu}$ and $\boldsymbol{\sigma}$ are tensors of reluctivity and conductivity, respectively; ∇ is the vector differential operator; ω_s is the angular frequency of stator field; j is the imaginary unit.

Only $\underline{\boldsymbol{J}}_\mathrm{s}$ was considered in the stator windings. In the other conductive regions, $\mathrm{j}\omega_\mathrm{s}\boldsymbol{\sigma} \cdot \underline{\boldsymbol{A}}$ was used. In the nonconductive regions, no current density. Moreover, in the rotary parts, the tensor of conductivity was $s\boldsymbol{\sigma}$, where s means slip, so only one frequency, ω_s, was assigned for the whole simulation.

A weak form was used in the FEA. Using the shape function $\boldsymbol{N}_\mathrm{e}$ of edge-based elements as a weight function, i.e., Galerkin's method, deduced the weak form of (1) as

$$\iiint_\Omega [\boldsymbol{\nu} \cdot (\nabla \times \underline{\boldsymbol{A}}) \cdot (\nabla \times \boldsymbol{N}_\mathrm{e}) - \boldsymbol{N}_\mathrm{e} \cdot \underline{\boldsymbol{J}}_\mathrm{s} + \mathrm{j}\omega_\mathrm{s}\boldsymbol{N}_\mathrm{e} \cdot (\boldsymbol{\sigma} \cdot \underline{\boldsymbol{A}})]\,\mathrm{d}\Omega - \oiint_\Gamma \boldsymbol{N}_\mathrm{e} \cdot [\boldsymbol{\nu} \cdot (\nabla \times \underline{\boldsymbol{A}}) \times \boldsymbol{n}]\,\mathrm{d}\Gamma = 0 \tag{2}$$

where Ω is the corresponding domain; Γ is the boundary of Ω; $\boldsymbol{n}$ is the outward-directed normal unit vector on a boundary.

In the $r-\varphi-z$ cylindrical coordinate system shown in Fig. 2, a periodic condition was imposed in such a way that the components of the magnetic vector potential on two sides I and II, as pointed out in Fig. 2, that is, $\underline{A}_r^\mathrm{I}$, $\underline{A}_\varphi^\mathrm{I}$, and $\underline{A}_z^\mathrm{I}$ on side I, and $\underline{A}_r^\mathrm{II}$, $\underline{A}_\varphi^\mathrm{II}$, and $\underline{A}_z^\mathrm{II}$ on side II, fulfilled the condition: $\underline{A}_r^\mathrm{I} = (-1)^k \underline{A}_r^\mathrm{II}$, $\underline{A}_\varphi^\mathrm{I} = (-1)^k \underline{A}_\varphi^\mathrm{II}$, and $\underline{A}_z^\mathrm{I} = (-1)^k \underline{A}_z^\mathrm{II}$, where k is the number of poles to be simulated. Another condition $\boldsymbol{n} \times \underline{\boldsymbol{A}} = \boldsymbol{0}$ was imposed on all the other sides.

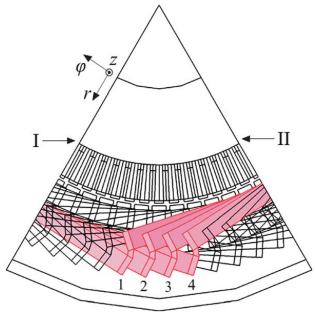

Fig. 2. Coil ends in a phase belt and the cylindrical coordinate system with the positive directions indicated.

The first-order edge-based elements, tetrahedra and prisms, were used in the end region and active region, respectively. The number of degrees of freedom was 301654.

C. Magnetic Forces and Force Densities

The magnetic forces, exerted on end-windings, are a typical case of Lorentz forces. The Lorentz force density $\boldsymbol{f}$ at a point in a current-carrying conductor is $\boldsymbol{f} = \boldsymbol{J} \times \boldsymbol{B}$, where $\boldsymbol{J}$ and $\boldsymbol{B}$ are the current density and magnetic induction.

In the Cartesian coordinate system, the phasors of the components of the current density are $\underline{J}_x$, $\underline{J}_y$, and $\underline{J}_z$, and the ones of the magnetic induction, $\underline{B}_x$, $\underline{B}_y$, and $\underline{B}_z$. From the above equation, the components of the force density at a point were

$$\begin{cases} f_x = 0.5\left[\mathrm{Re}\left\{\underline{J}_y\underline{B}_z{}^*\right\} - \mathrm{Re}\left\{\underline{J}_z\underline{B}_y{}^*\right\}\right] \\ \qquad + 0.5\left[\mathrm{Re}\{\underline{J}_y\underline{B}_z\mathrm{e}^{\mathrm{j}2\omega_\mathrm{s}t}\} - \mathrm{Re}\{\underline{J}_z\underline{B}_y\mathrm{e}^{\mathrm{j}2\omega_\mathrm{s}t}\}\right] \\ f_y = 0.5\left[\mathrm{Re}\left\{\underline{J}_z\underline{B}_x{}^*\right\} - \mathrm{Re}\left\{\underline{J}_x\underline{B}_z{}^*\right\}\right] \\ \qquad + 0.5\left[\mathrm{Re}\{\underline{J}_z\underline{B}_x\mathrm{e}^{\mathrm{j}2\omega_\mathrm{s}t}\} - \mathrm{Re}\{\underline{J}_x\underline{B}_z\mathrm{e}^{\mathrm{j}2\omega_\mathrm{s}t}\}\right] \\ f_z = 0.5\left[\mathrm{Re}\left\{\underline{J}_x\underline{B}_y{}^*\right\} - \mathrm{Re}\left\{\underline{J}_y\underline{B}_x{}^*\right\}\right] \\ \qquad + 0.5\left[\mathrm{Re}\{\underline{J}_x\underline{B}_y\mathrm{e}^{\mathrm{j}2\omega_\mathrm{s}t}\} - \mathrm{Re}\{\underline{J}_y\underline{B}_x\mathrm{e}^{\mathrm{j}2\omega_\mathrm{s}t}\}\right] \end{cases} \tag{3}$$

where f_x, f_y, and f_z denote instantaneous values of the components of the force density; Re means taking the real part of a complex number; $*$ means taking a conjugate complex number; and t is time. Obviously, in (3), each component is the sum of two components: a constant component and a sinusoidal component with a double-frequency, $2\omega_\mathrm{s}$.

Because the force density varied in the end-windings, the force on segment i of a coil end was computed by integrating (3) on its volume V_i as $\boldsymbol{F}_i = \iiint_{V_i} \boldsymbol{f}\mathrm{d}V_i$, where $\boldsymbol{F}_i$ denotes the force on segment i. Moreover, the force $\bar{\boldsymbol{F}}_i$ was assumed to be exerted on the centre (x_i, y_i, z_i) of segment i.

The force $\boldsymbol{F}_i$ was then expressed in the cylindrical coordinate system marked in Fig. 2. The z-component of the force was the same as in the Cartesian coordinate system, whereas the r- and φ-components, $F_{i,r}$ and $F_{i,\varphi}$, were obtained by

$$\begin{cases} F_{i,r} = \sqrt{F_{i,x}^2 + F_{i,y}^2}\cos\left[\mathrm{atan2}(F_{i,y}, F_{i,x}) - \mathrm{atan2}(y_i, x_i)\right] \\ F_{i,\varphi} = \sqrt{F_{i,x}^2 + F_{i,y}^2}\sin\left[\mathrm{atan2}(y_i, x_i) - \mathrm{atan2}(F_{i,y}, F_{i,x})\right] \end{cases} \tag{4}$$

where atan2 is the four-quadrant inverse tangent function; and $F_{i,x}$ and $F_{i,y}$ are the x- and y-components of $\boldsymbol{F}_i$, respectively.

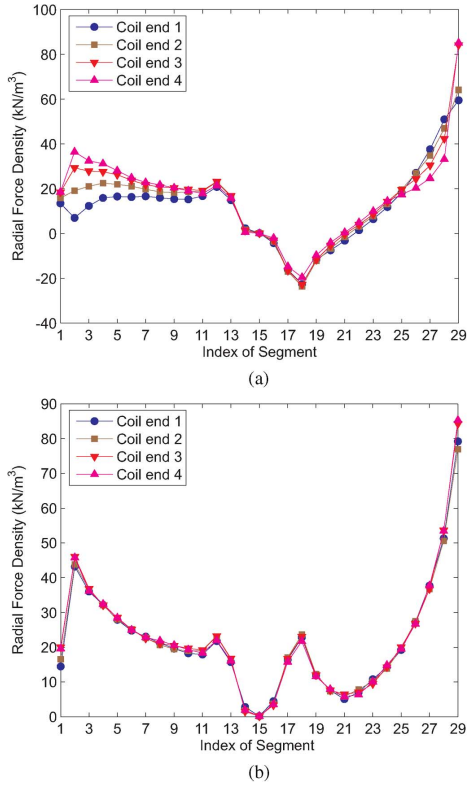

Fig. 3. Average radial force density in the segments of the coil ends in a phase belt: (a) the constant component, $F_{i,r,\_}/V_i$; (b) the amplitude of the sinusoidal component, $\hat{F}_{i,r,\sim}/V_i$.

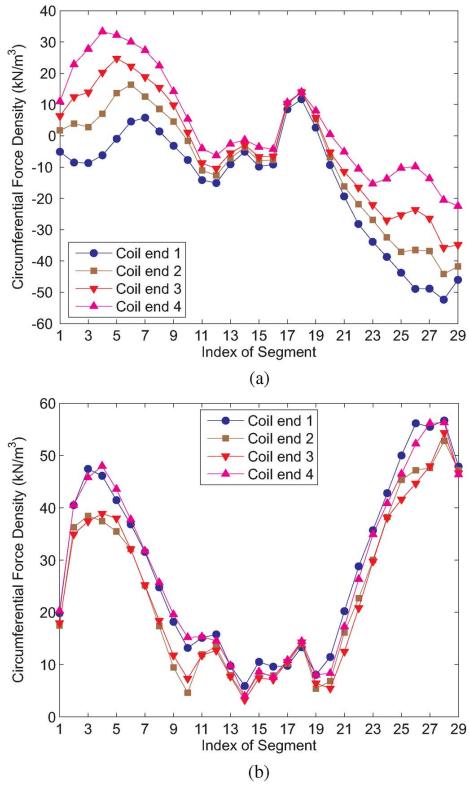

Fig. 4. Average circumferential force density in the segments of the coil ends in a phase belt: (a) the constant component, $F_{i,\varphi,\_}/V_i$; (b) the amplitude of the sinusoidal component, $\hat{F}_{i,\varphi,\sim}/V_i$.

Then the force $\boldsymbol{F}_i$ was transformed into

$$\begin{cases} F_{i,r} = F_{i,r,\_} + \hat{F}_{i,r,\sim}\cos(2\omega_s t + \vartheta_{i,r0}) \\ F_{i,\varphi} = F_{i,\varphi,\_} + \hat{F}_{i,\varphi,\sim}\cos(2\omega_s t + \vartheta_{i,\varphi 0}) \\ F_{i,z} = F_{i,z,\_} + \hat{F}_{i,z,\sim}\cos(2\omega_s t + \vartheta_{i,z0}) \end{cases} \tag{5}$$

where $F_{i,r,\_}$, $F_{i,\varphi,\_}$, and $F_{i,z,\_}$, and $\hat{F}_{i,r,\sim}$, $\hat{F}_{i,\varphi,\sim}$, and $\hat{F}_{i,z,\sim}$ are the constant components and the amplitudes of the sinusoidal components of the r-, φ-, and z-components of the force, respectively; and $\vartheta_{i,r0}$, $\vartheta_{i,\varphi 0}$, and $\vartheta_{i,z0}$ are the phase angles of the corresponding sinusoidal components.

As the volume of each segment was not equal, for the sake of comparison, the average force density in segment i, $\boldsymbol{f}_i$, was introduced and defined as $\boldsymbol{f}_i = \boldsymbol{F}_i/V_i$. The components of the average force density, $f_{i,r}$, $f_{i,\varphi}$, and $f_{i,z}$, were written in

$$\begin{cases} f_{i,r} = \frac{F_{i,r,\_}}{V_i} + \frac{\hat{F}_{i,r,\sim}}{V_i}\cos(2\omega_s t + \vartheta_{i,r0}) \\ f_{i,\varphi} = \frac{F_{i,\varphi,\_}}{V_i} + \frac{\hat{F}_{i,\varphi,\sim}}{V_i}\cos(2\omega_s t + \vartheta_{i,\varphi 0}) \\ f_{i,z} = \frac{F_{i,z,\_}}{V_i} + \frac{\hat{F}_{i,z,\sim}}{V_i}\cos(2\omega_s t + \vartheta_{i,z0}). \end{cases} \tag{6}$$

III. Results and Analysis

The phase belt in Fig. 2 was analyzed since the other phase belts would have similar situations. Here, the average force densities were studied but the results were fit for the forces.

Three groups of coefficients in (6), i.e., $F_{i,r,\_}/V_i$ and $\hat{F}_{i,r,\sim}/V_i$, $F_{i,\varphi,\_}/V_i$ and $\hat{F}_{i,\varphi,\sim}/V_i$, and $F_{i,z,\_}/V_i$ and $\hat{F}_{i,z,\sim}/V_i$, were computed at full load and are plotted in Figs. 3–5, respectively.

In Fig. 3, from the values of $F_{i,r,\_}/V_i$, it is clear that $F_{i,r,\_}/V_i$ in the four coil ends, except in segments 15–21 of the four coil ends, lies in positive r-direction. Besides, in most knuckle parts of the four coil ends, i.e., segments 2, 28, and 29, both $F_{i,r,\_}/V_i$ and $\hat{F}_{i,r,\sim}/V_i$ are stronger than the other parts.

In Fig. 4, except the lower part of coil end 1, $F_{i,\varphi,\_}/V_i$ in the lower parts of the other coil ends almost lies in positive φ-direction. In the upper parts of all the coil ends, $F_{i,\varphi,\_}/V_i$ is in negative φ-direction. Furthermore, both $F_{i,\varphi,\_}/V_i$ and $\hat{F}_{i,\varphi,\sim}/V_i$ are larger in most knuckle parts and their neighboring involute parts of all the coil ends, i.e., segments 2–7 and 23–29. Also, as to $F_{i,\varphi,\_}/V_i$, its distribution in the four coil ends is different. However, with respect to $\hat{F}_{i,\varphi,\sim}/V_i$, its distribution, in inner coil ends 2 and 3, and in outer coil ends 1 and 4, is nearly similar, respectively.

In Fig. 5, it can be seen that $F_{i,z,\_}/V_i$ lies in positive z-direction except in the lower part of coil end 1 and segments 10 and 11 of coil ends 2–4. $F_{i,z,\_}/V_i$ and $\hat{F}_{i,z,\sim}/V_i$ in most knuckle parts and a part of the involute parts, i.e., segments 2–6, 23–28 as well as 15, are larger than in the other parts.

In Figs. 3–5, the three groups of coefficients mentioned above have almost equal magnitudes in each segment.

The radial and circumferential sinusoidal components of the forces are usually of interest. Fig. 6 plots these force densities in each segment of coil end 1, from which the phase difference can be seen. The absolute value of the phase difference, $|\vartheta_{i,r0} - \vartheta_{i,\varphi 0}|$, was considered. For instance, in segments 2 and 6, $|\vartheta_{i,r0} - \vartheta_{i,\varphi 0}| < \pi/2$, whereas in segments 24 and 28,

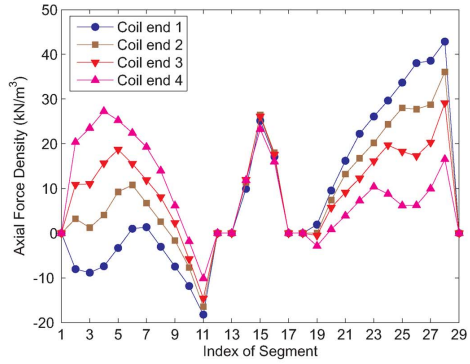

(a)

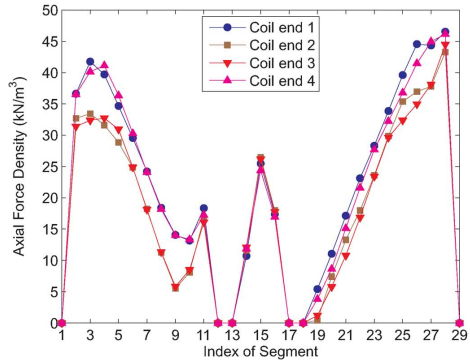

(b)

Fig. 5. Average axial force density in the segments of the coil ends in a phase belt: (a) the constant component, $F_{i,z,\_}/V_i$; (b) the amplitude of the sinusoidal component, $\hat{F}_{i,z,\sim}/V_i$.

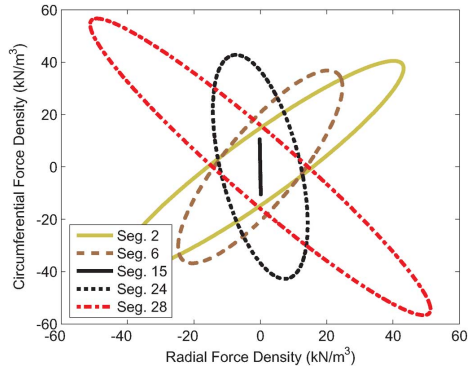

Fig. 6. The relations between the radial and circumferential sinusoidal components of the average force density in coil end 1, $(\hat{F}_{i,r,\sim}/V_i)\cos(2\omega_s t+\vartheta_{i,r0})$ and $(\hat{F}_{i,\varphi,\sim}/V_i)\cos(2\omega_s t+\vartheta_{i,\varphi 0})$.

$\pi/2<|\vartheta_{i,r0}-\vartheta_{i,\varphi 0}|<\pi$. In fact, in most of the lower part of a coil end, $|\vartheta_{i,r0}-\vartheta_{i,\varphi 0}|<\pi/2$, whereas in most of the upper part, $\pi/2<|\vartheta_{i,r0}-\vartheta_{i,\varphi 0}|<\pi$. A straight line for segment 15 means $|\vartheta_{i,r0}-\vartheta_{i,\varphi 0}|\approx\pi$.

The von Mises stresses in the copper coil ends, related to the constant components of the forces, were analyzed and listed in Table II. The yield strength and tensile strength for copper are 69 MPa and 220 MPa, respectively. The computed stresses in Table II are much smaller. The stresses, related to the sinusoidal components of the forces, rely on the damping of the end-windings that usually comes from the measurement.

TABLE II
ANALYSIS OF VON MISES STRESSES IN COIL ENDS

	Maximum stress (MPa)	Region with larger stresses
Coil end 1	0.353	Segments 15, 23, 24, 29
Coil end 2	0.392	Segments 15, 29
Coil end 3	0.402	Segments 1, 15, 29
Coil end 4	0.386	Segments 1, 2, 6, 7, 15

IV. CONCLUSION

This paper studies the steady-state magnetic forces on the end-windings. Generally, in r-, φ-, and z-directions, the constant components of the forces on the upper part are stronger than those on the lower part of a coil end. The amplitudes of the sinusoidal components, in r-, φ-, and z-directions, are also larger in the upper part. Inside a phase belt, the constant components and the amplitudes of the sinusoidal components of the forces on the same positions of different coil ends are almost different. Besides, the phase difference between the radial and circumferential sinusoidal components on the upper part is different from that on the lower part of a coil end.

In addition, the forces on different positions of a single coil end are different. With respect to a coil end, the knuckle part and its neighboring parts are subject to larger instantaneous forces than the other parts. However, the stresses in a coil end, corresponding to the constant components of the forces, are small in comparison with the yield strength of copper.

REFERENCES

[1] D. J. Scott, S. J. Salon, and G. L. Kusik, "Electromagnetic forces on the armature end windings of large turbine generators I—Steady state conditions," *IEEE Trans. Power App. Syst.*, vol. PAS-100, no. 11, pp. 4597–4603, Nov. 1981.

[2] S. J. Salon, D. J. Scott, and G. L. Kusic, "Electromagnetic forces on the end windings of large turbine generators. II. Transient conditions," *IEEE Trans. Power App. Syst.*, vol. PAS-102, no. 1, pp. 14–19, Jan. 1983.

[3] S. Williamson and M. R. E. Ellis, "Influence of rotor currents on end-winding forces in cage motor," *Proc. IEE*, vol. 135, no. 6, pp. 371–379, Nov. 1988.

[4] P. J. Lawrenson, "Forces on turbogenerator end windings," *Proc. IEE*, vol. 112, no. 6, pp. 1144–1158, Jun. 1965.

[5] M. Ohtaguro, K. Yagiuchi, and H. Yamaguchi, "Mechanical behavior of stator endwindings," *IEEE Trans. Power App. Syst.*, vol. PAS-99, no. 3, pp. 1181–1185, May/Jun. 1980.

[6] A. Merkhouf, B. F. Boueri, and H. Karmaker, "Generator end windings forces and natural frequency analysis," in *Proc. IEEE Int. Elect. Mach. Drives Conf.*, Jun. 2003, vol. 1, pp. 111–114.

[7] J. T. Park, K. C. Kim, and J. I. Lee, "Calculation of the end winding force for electrical rotating machines," in *Proc. IEEE Int. Elect. Mach. Drives Conf.*, Jun. 2003, vol. 3, pp. 1640–1645.

[8] G. K. M. Khan, G. W. Buckley, and N. Brooks, "Calculation of forces and stresses on generator end-windings—Part I: Forces," *IEEE Trans. Energy Convers.*, vol. 4, no. 4, pp. 661–670, Dec. 1989.

[9] X. Wen, R. Yao, and J. A. Tegopoulos, "Calculation of forces on the stator end windings of turbogenerator by the transient quasi-3D method," *IEEE Trans. Magn.*, vol. 32, no. 3, pp. 1669–1672, May 1996.

[10] D. Ban, D. Žarko, and I. Mandić, "Turbogenerator end-winding leakage inductance calculation using a 3-D analytical approach based on the solution of Neumann integrals," *IEEE Trans. Energy Convers.*, vol. 20, no. 1, pp. 98–105, Mar. 2005.

[11] M. T. Holmberg, "Three-dimensional finite element computation of eddy currents in synchronous machines," Ph.D. dissertation, Chalmers Univ. Technology, Gothenburg, Sweden, Dec. 1998.

Manuscript received February 29, 2008. Current version published December 17, 2008. Corresponding author: R. Lin (e-mail: ranran.lin@gmail.com).